

JCU ePrints

This file is part of the following reference:

**Cole, David (2007) *The splashing morphology of liquid-liquid impacts.*
PhD thesis, James Cook University.**

Access to this file is available from:

<http://eprints.jcu.edu.au/2065>



CHAPTER 6 - BUBBLE ENTRAPMENT

6.1 Introduction

The formation of bubbles in liquid-liquid impacts can be broken into three main groups:

1. Bubbles formed on initial drop impact
 - Thoroddsen bubbles
 - Oguz bubble rings
2. Bubbles formed due to cavity collapse
 - Primary bubble entrapment
 - Secondary bubble entrapment
3. Bubbles formed from thin film rupture
 - Film thinning and rupture due to drainage
 - Film thinning and rupture due to rapid expansion

In this chapter further investigation into each mode of bubble entrapment will be conducted, with special attention being paid to the formation of microbubbles. The reason for this is that in most practical applications, like water aeration, extremely small bubbles ($<150\ \mu\text{m}$) play a significant role in oxygen exchange with the bulk fluid. The high internal pressure of a microbubble assists in the mass diffusion of air into the solution. Furthermore, a swarm of these microbubbles will have a greater surface area for mass diffusion compared to one large bubble of similar volume. Single large bubbles also have a tendency to burst at the free surface rather than diffuse into the bulk fluid, making them less desirable. Finally, the small size of microbubbles makes them ideal candidates to be transported deep into the solution via vortex ring motion. For practical purposes, it is also useful to predict under what conditions the microbubbles will be carried into the bulk fluid and if possible, to quantify the amount of air and ultimately oxygen they will transfer. The discussion will start by examining the bubbles that form from initial impact.

6.2 Bubbles from Initial Impact

6.2.1 Thoroddsen bubbles

Two different modes of microbubble entrapment phenomena have been shown to occur upon initial impact. The first mode of bubble entrapment is the formation of Thoroddsen bubbles. Thoroddsen bubbles are formed during the initial moments of contact between the drop and free surface (Thoroddsen *et al.* 2003). Thoroddsen *et al.* (2003) went on to show how the bubbles form as the result of an instability associated with an entrapped disk of air. However, there are a few remaining questions to be answered in regards to this phenomena. What volume of air do Thoroddsen bubbles entrap? What are the limits on this phenomenon in terms of Froude and Weber number? To answer the first question, the 20g-01 data set was examined and the resulting bubble(s) from each impact measured and plotted on Figure 6.1. The volume of each of each bubble was determined and added so the total volume of air for each impact can be computed (Figure 6.2). The Thoroddsen bubbles observed in this series of impacts ranged in size from 0.06 – 0.12 mm in diameter. It is salient to note that two Thoroddsen bubbles are not always formed on impact. Sometimes only one bubble was formed.

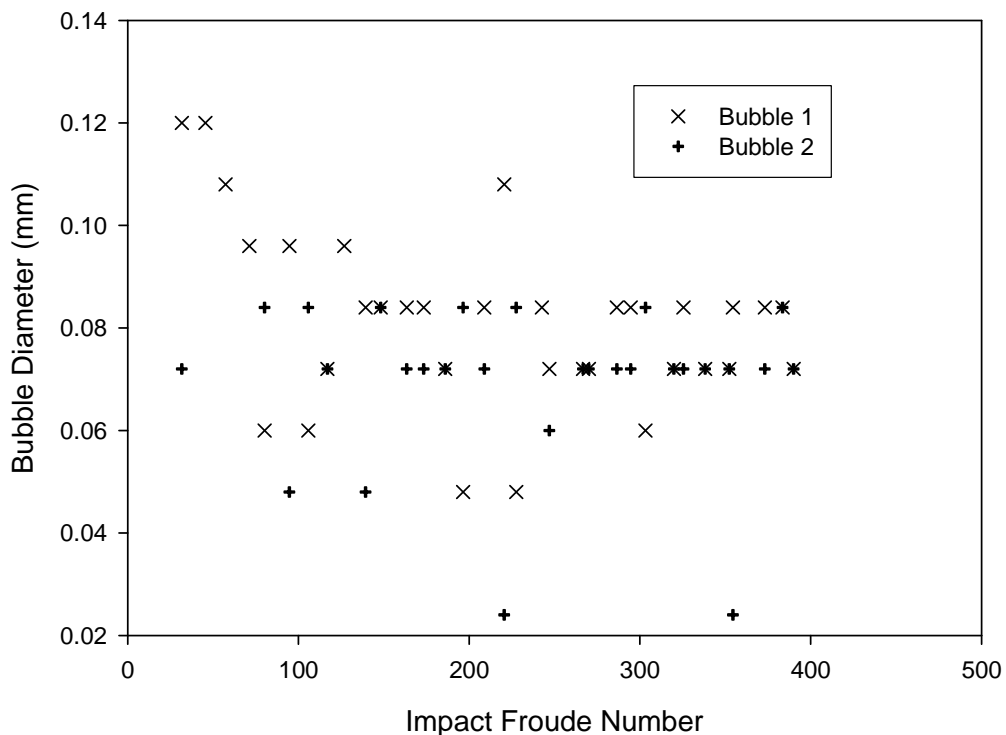


Figure 6.1 Thoroddsen bubble sizes from the impacts from 3.2 mm drops (20g needles)

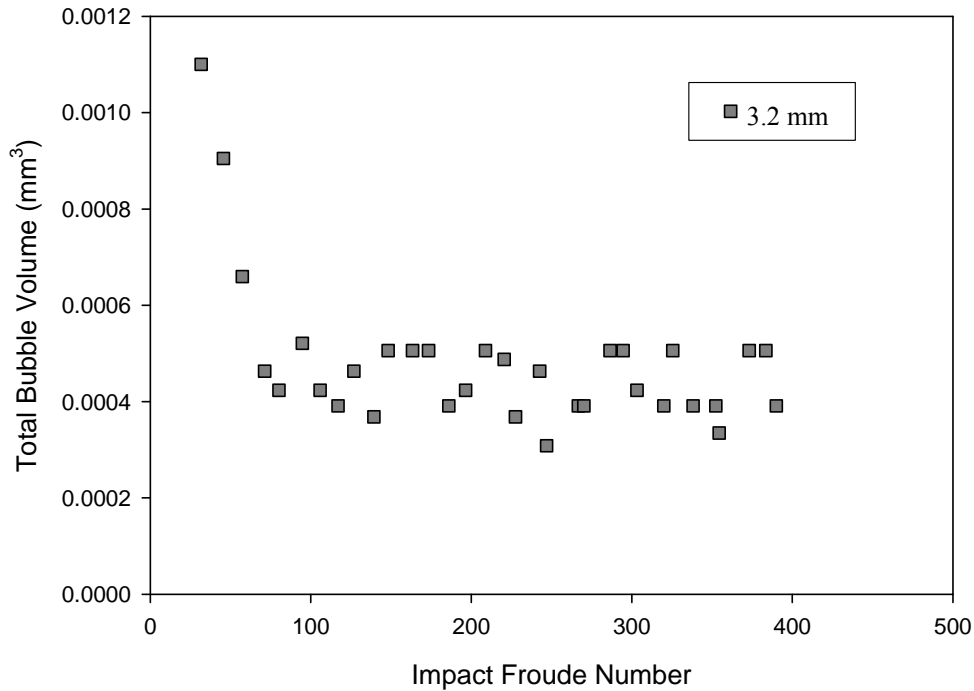


Figure 6.2 Total volume of the Thoroddsen bubbles formed from 3.2 mm drops (20g needles)

Examining Figure 6.2 the total volume entrapped air at the lower impact velocities is higher than the volume of air entrapped at higher impact velocities. From $Fr > 80$ the total quantity of air entrapped becomes roughly constant with an average of 0.00044 mm^3 . It is interesting to note that as the impact Froude number decreases larger quantities of air become entrapped. Therefore, it is probable that if the Froude and Weber number are reduced further, the quantity of air entrapped will increase. One can postulate that the size of the air sheet will grow until the air layer prevents the liquid surfaces from coalescing. The entrainment of an air film between the two liquids leads to the microbubble formation seen in the primary microbubble entrainment regime. Thus, the lower limit on the formation of Thoroddsen bubbles is directly connected to the upper limit of the primary microbubble entrainment regime.

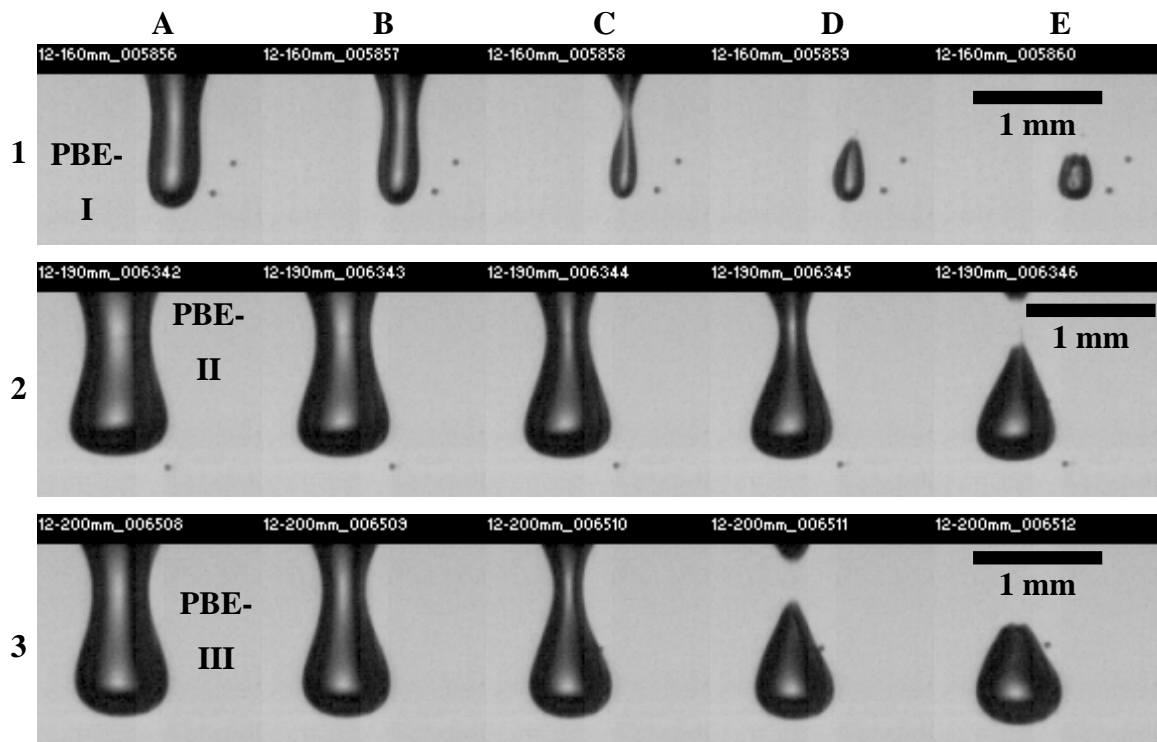
6.3 Bubbles Formed During Cavity Collapse

6.3.1 Primary bubble entrapment

The second major mode of bubble entrapment is a result of cavity collapse to entrap a bubble in the bulk fluid. Extensive research already exists in this area. Here the variation of bubble size and shape vary with impact velocity will be examined. Figure 6.3 show a variety of different Froude number impacts and the bubble size and shape of the entrapped bubble.

Table 6.1 Impact conditions for the image sequences shown in Figure 6.3

Sequence Number	Sequence Name	Drop Size (D) (mm)	Drop Velocity (U) (m/s)	Froude Number	Weber Number	Reynolds Number	t_c (D/U) (ms)
PBE-I	33g-12-160	2.13	2.02	186	114	3749	1.08
PBE-II	33g-12-190	2.14	2.11	212	130	4022	1.01
PBE-III	33g-12-200	2.16	2.16	221	137	4139	0.99
PBE-IV	33g-12-220	2.15	2.23	236	147	4284	0.96
PBE-V	33g-12-230	2.14	2.28	246	152	4346	0.94
PBE-VI	33g-12-260	2.15	2.38	269	166	4546	0.90
PBE-VII	33g-12-280	2.14	2.46	287	175	4683	0.87
PBE-VIII	33g-12-290	2.14	2.52	303	186	4815	0.85
PBE-IX	33g-12-320	2.15	2.62	317	193	5014	0.82
PBE-X	33g-12-340	2.15	2.69	342	201	5142	0.80



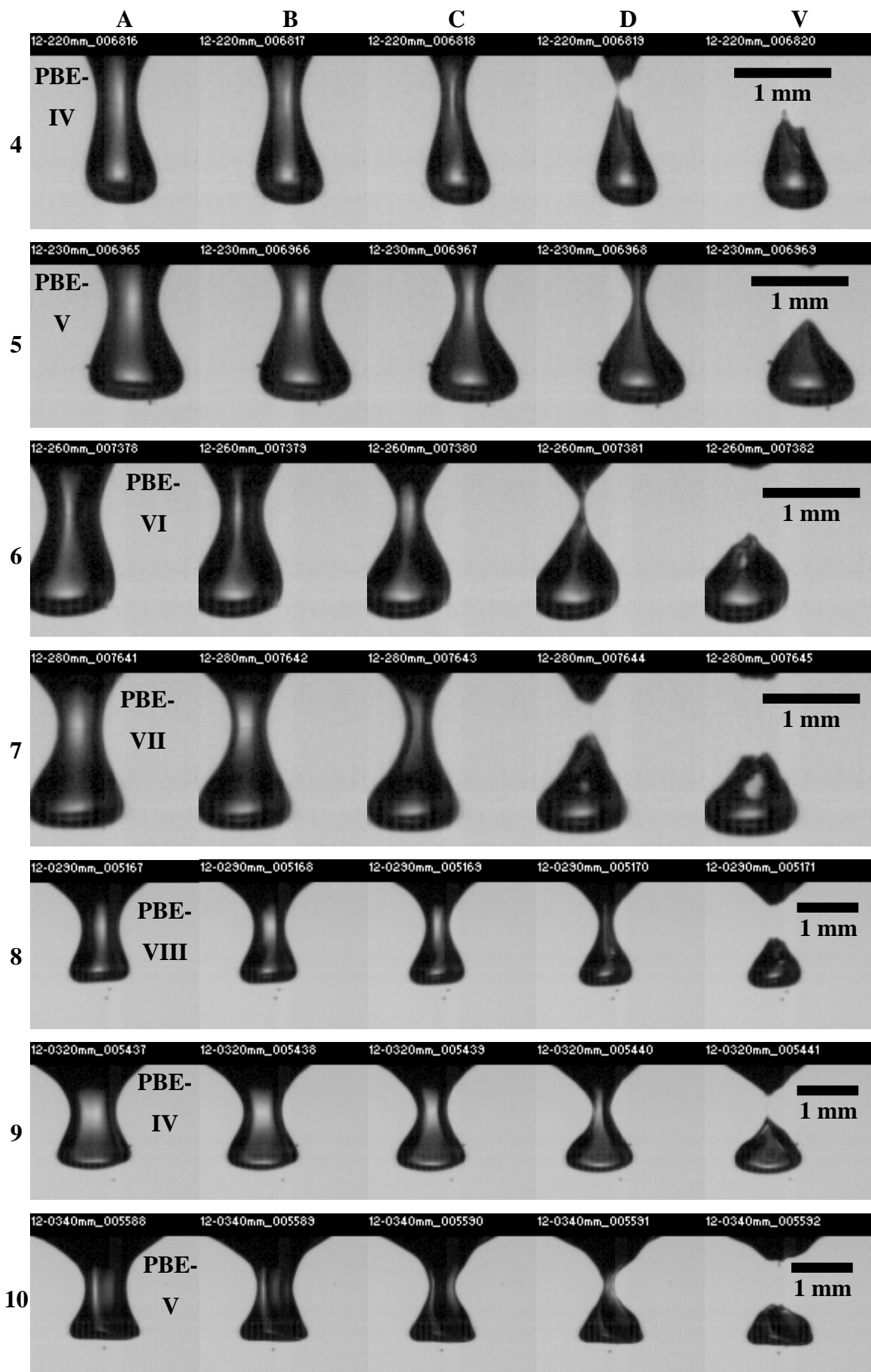


Figure 6.3 A series of impacts showing the shape of the bubble formed from primary bubble entrapment

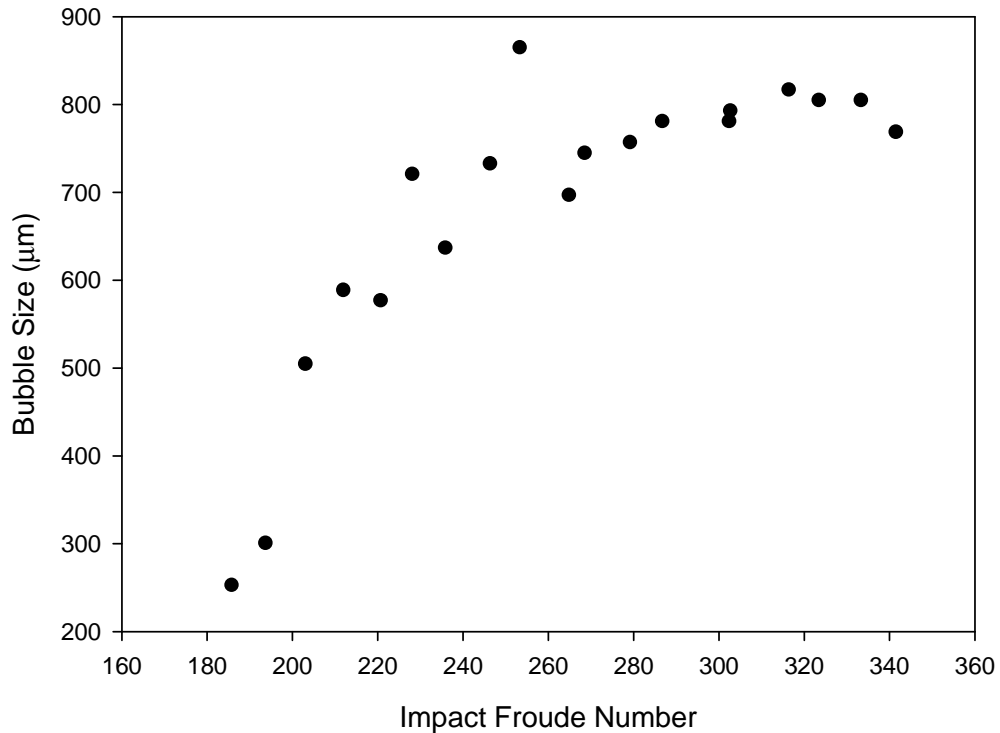


Figure 6.4 Plot of entrapped bubble size versus Froude number

Examining Figure 6.3 and Figure 6.4 general trends in bubble shape and size as the impact Froude number varies can be ascertained. At lower impact velocities small bubbles in the order of 250 µm in diameter are formed. While at the upper end of the primary bubble entrapment regime the bubbles are more than three times this diameter at 800 µm. There also appears to be a point where the bubble size reaches a peak before declining in size towards the very end of the primary bubble entrapment regime. In terms of bubble shape, some interesting trends occur across this regime. At the lower impact velocities, the bubble shape is almost cylindrical as it snaps off the cavity base Figure 6.3 (1). Moving higher into the primary bubble entrapment regime Figure 6.3 (2-4) the bubbles width begins to increase with a relatively constant curvature around the base and sides of the bubble. At even higher impact Froude numbers, Figure 6.3 (5-9), the aspect ratio of the bubble increases and the curvature along the base of the bubble decreases markedly. This results in bubbles that have an almost flat base. In Figure 6.3 (10) the entrapped bubble has an almost perfectly flat base which gives the bubble a distinct cone shape.

6.3.2 Multiple bubble primary bubble entrapment

In the transition between the primary bubble entrapment regime and the post-entrapment jetting regime, there exists a narrow Fr-We range where multiple bubbles can be formed when the cavity collapses. There is scant reference to this behaviour in literature. Rein (1996) showed an example of this phenomenon but suggested that it was a random event due to surface waves causing an asymmetric collapse. Elmore *et al.* (2001) also presented some images of what appeared to be multiple bubble entrapment but they were unclear. Thus since this phenomena has not been adequately described in current literature a comprehensive examination of this flow behaviour will be carried out here. A series of different images sequences showing the different entrapment phenomena that can occur in this range are shown in Figure 6.5 to Figure 6.9.

Table 6.2 Impact conditions for multiple bubble entrapment

Sequence Number	Sequence Name	Drop Size (D) (mm)	Drop Velocity (U) (m/s)	Froude Number	Weber Number	Reynolds Number	t_c (D/U) (ms)
MBE-I	33g-07-360	2.09	2.61	332	194	4824	0.80
MBE-II	33g-07-362	2.09	2.61	332	194	4824	0.80
MBE-III	33g-07-380	2.06	2.63	343	195	4826	0.78
MBE-IV	33g-07-382*	2.06	2.64	345	196	4841	0.78
MBE-V	33g-07-388	2.06	2.68	356	202	4904	0.77

* The initial impact 33g-07-382 was not captured thus these values are estimates

In the first image sequence (Figure 6.5) the bubble entrapment mode associated with the primary bubble entrapment regime can be seen. The base of the cavity just before entrapment begins to arch upward due to surface tension driven instabilities. The bubble that forms takes the shape of a horizontal cylinder with an approximate height of 1 mm and diameter of 400 μm . In Figure 6.5 (B5-E5) the downward jet attempts to split the bubble in two and a thin bridge between the two halves of the bubble forms. However, the downward jet does not have sufficient strength of overcome the surface tension forces binding the bubbles together. Thus, in Figure 6.5 (A6-E6) the surface tension forces begin to restore the bubble to a spherical shape. The bridge begins to thicken and a single spherical bubble forms after sometime.

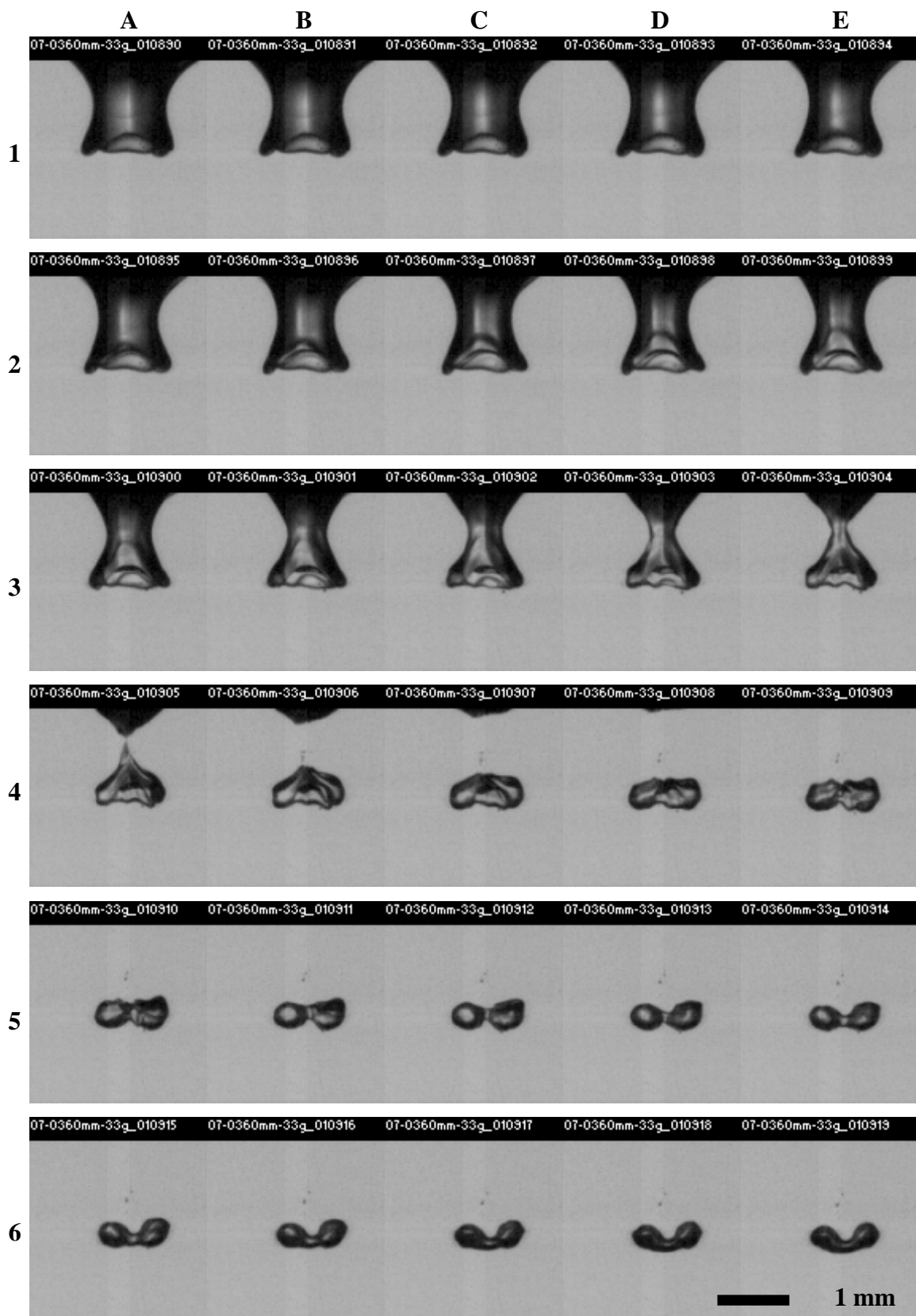


Figure 6.5 Below surface images for MBE-I ($Fr = 332$, $We = 194$, $Re = 4824$, $t_c = 0.8$)
(40000 FPS)

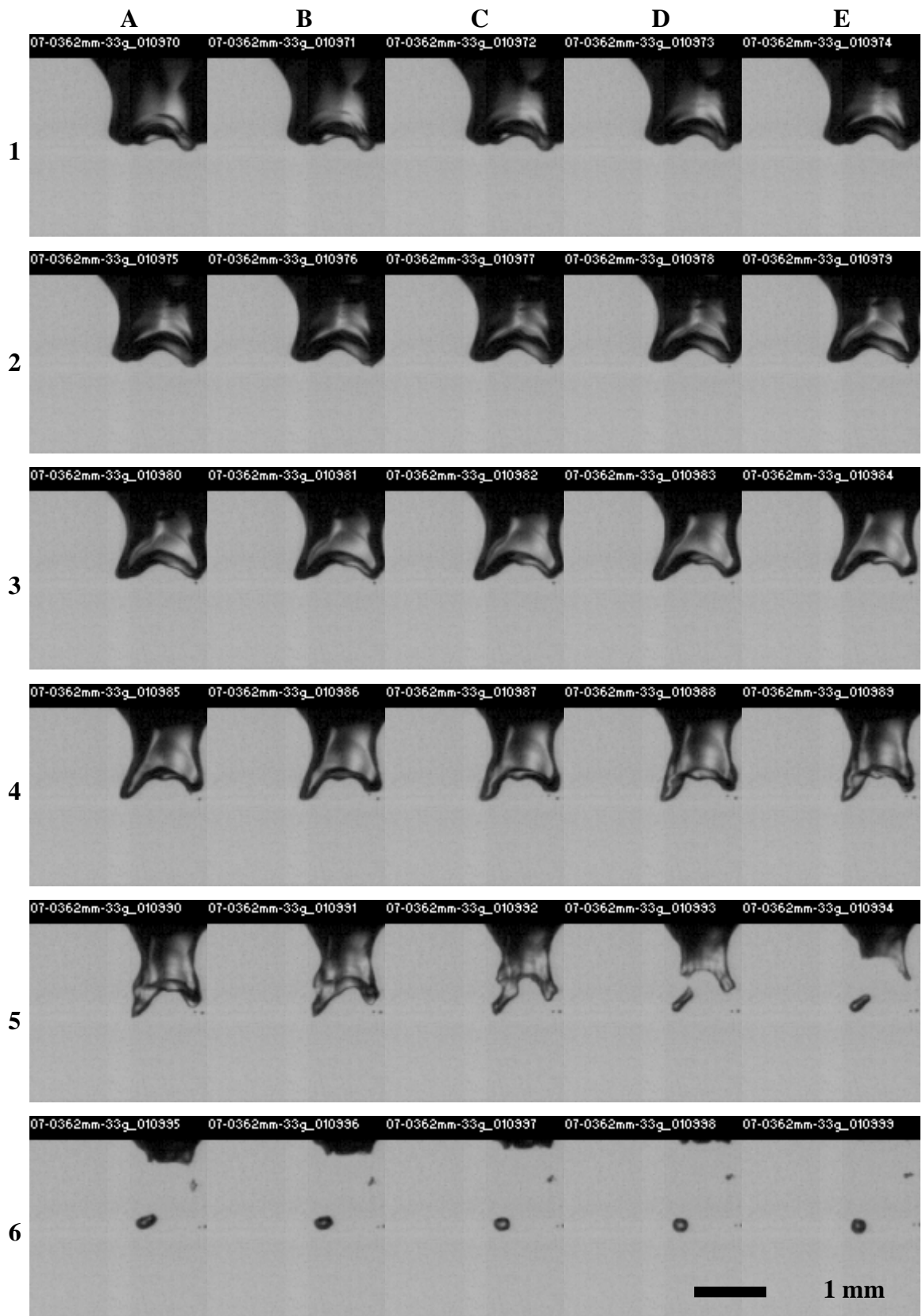


Figure 6.6 Below surface images for MBE-II ($Fr = 332$, $We = 194$, $Re = 4824$, $t_c = 0.8$) (40000 FPS)

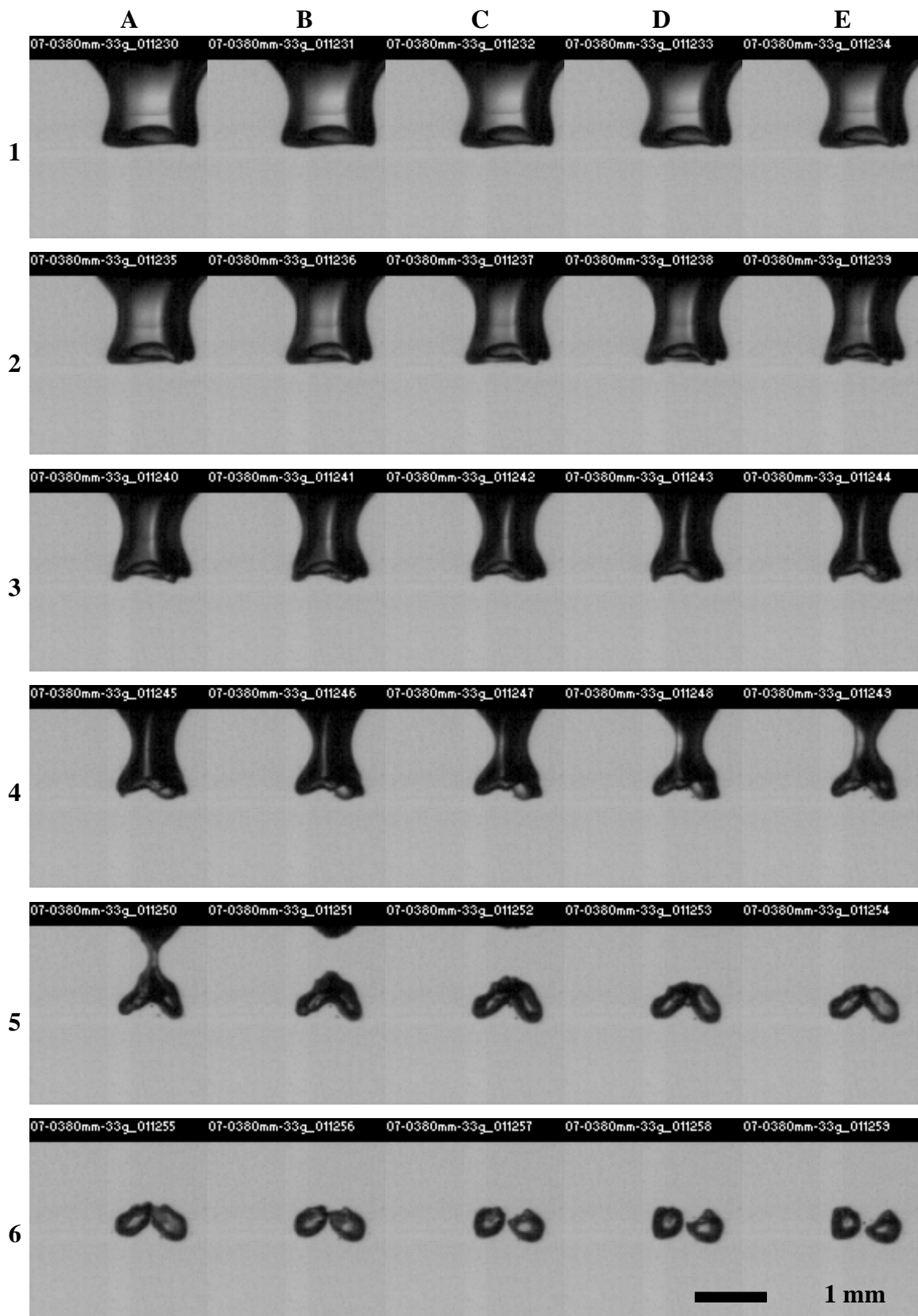


Figure 6.7 Below surface images for MBE-III ($Fr = 343$, $We = 195$, $Re = 4826$, $t_c = 0.78$) (40000 FPS)

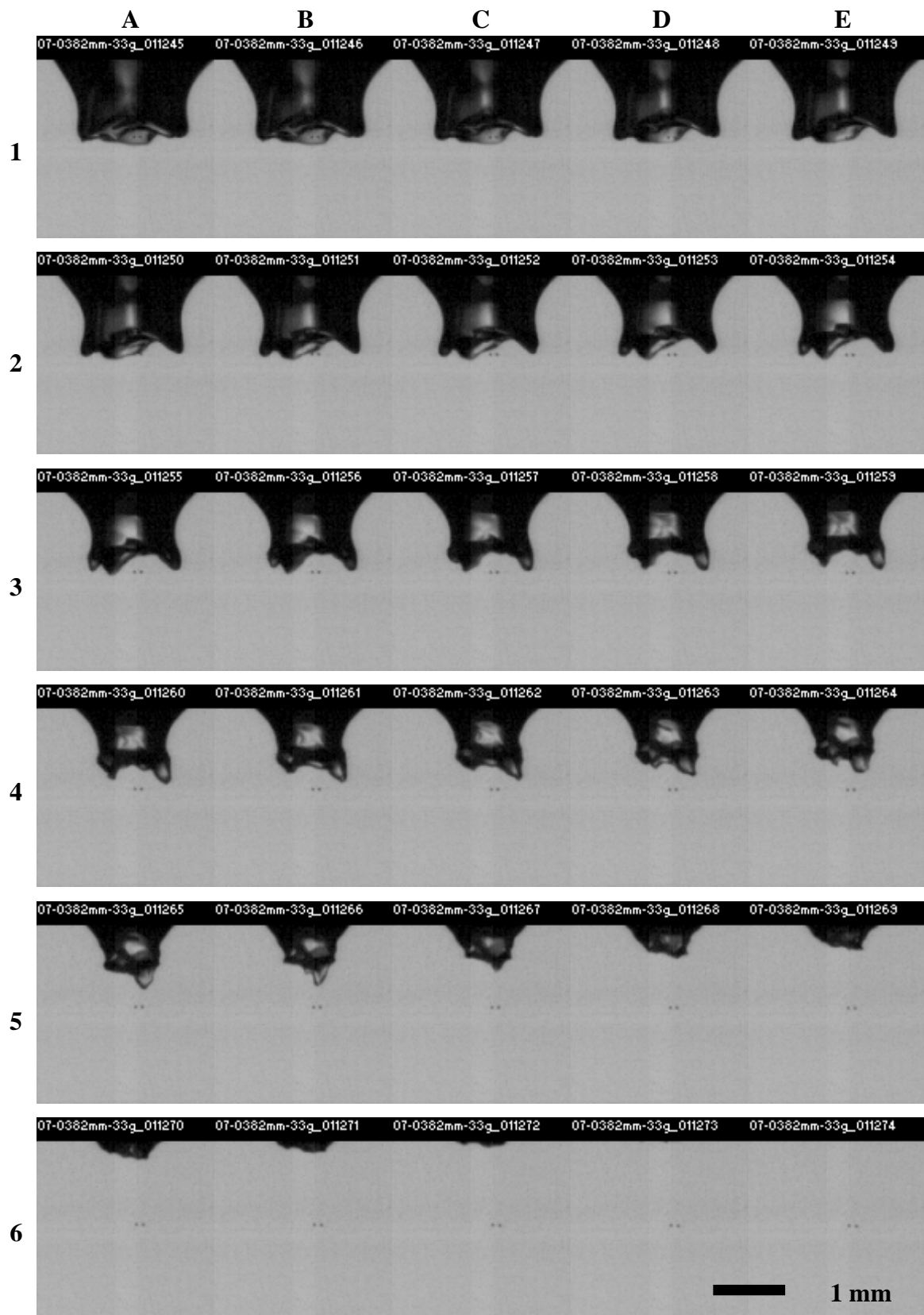


Figure 6.8 Below surface images for MBE-IV ($Fr = 345$, $We = 196$, $Re = 4841$, $t_c = 0.78$) (40000 FPS)

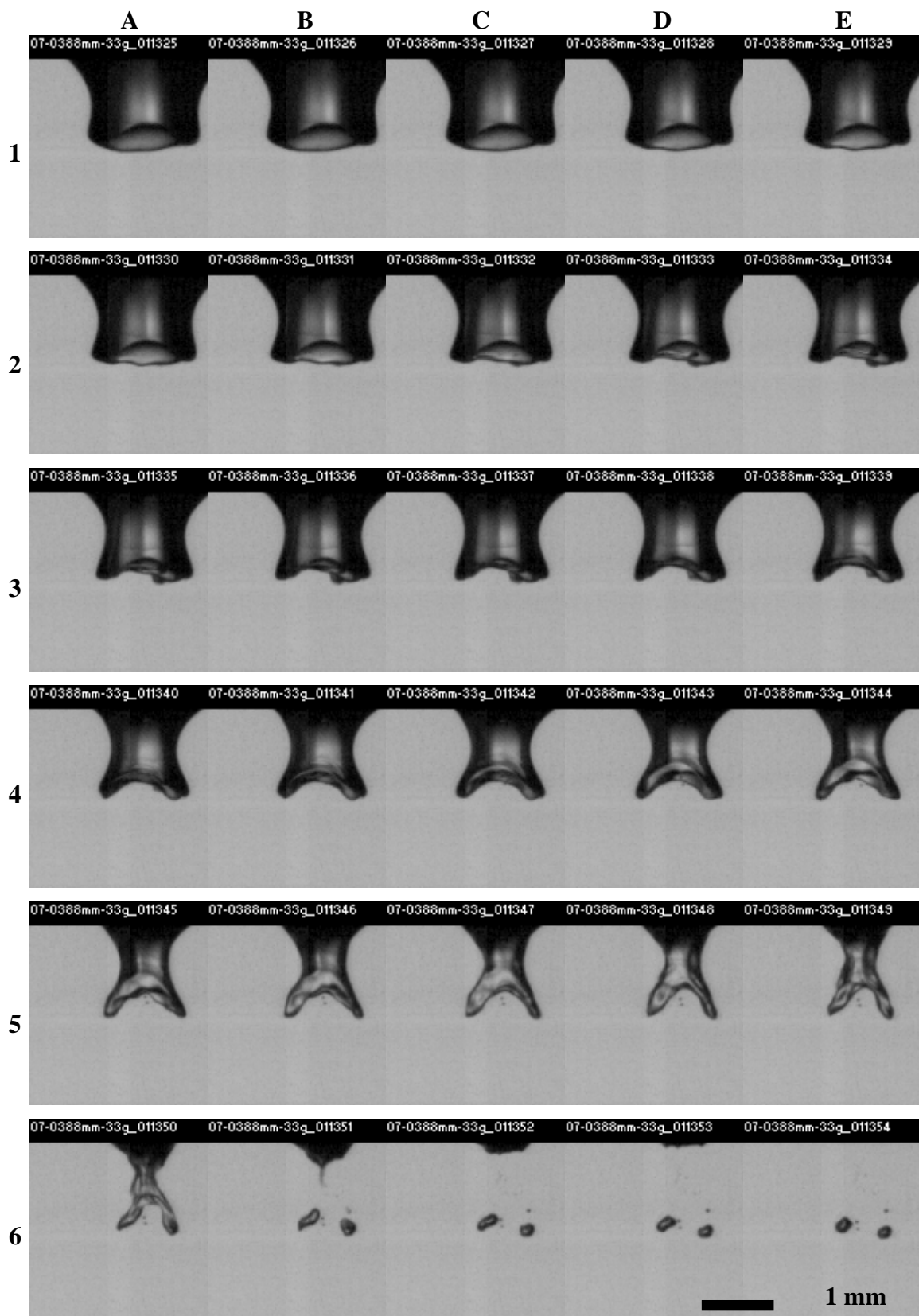


Figure 6.9 Below surface images for MBE-V ($Fr = 356$, $We = 202$, $Re = 4904$, $t_c = 0.77$) (40000 FPS)

The event shown in Figure 6.7 illustrates once again how one large bubble forms after snap off like in Figure 6.5. Surface tension driven instabilities give the cavity base a complex 3D structure with significant arching along the centreline present. However, what makes this case different is that the downward jet has sufficient strength to split the single large bubble into two smaller bubbles about 460 μm in diameter (Figure 6.7 (C6)). These two smaller bubbles do not remerge to form a single bubble and are driven towards the free surface via buoyancy forces where they burst.

Figure 6.6 demonstrates a slightly different mode of bubble entrapment than the ones mentioned previously. Here the base of the cavity retracts before the walls of the cavity close. This results in a very distinct arch structure at the base of the cavity. The shape of this arch is strikingly similar to the numerical simulations of Oguz and Prosperetti (1991). The left side of the cavity tip breaks up to form a bubble 220 μm in diameter (Figure 6.6 (D5)). Moments later in Figure 6.6 (A6) the right side of the cavity tip breaks up to form a 100 μm diameter bubble. This type of bubble formation can also be seen in Figure 6.9. Like the previous example, the stem of the cavity breaks up due to surface tension instabilities. These instabilities arise because a purely surface tension driven collapse is inherently unstable (Birkhoff 1956).

In other examples like Figure 6.8 the stem again becomes unstable but it appears the direction of the converging flow is directed upwards such that the entire stem is driven into the cavity without breaking up and gives rise to a thick jet. Therefore, in this regime there appears to be a delicate balance between the direction of the converging flow at the tip of the cavity and surface tension driven instabilities. These surface tension driven instabilities leads to the somewhat variable behaviour of the phenomena.

6.3.3 Secondary Bubble Entrapment

In several impacts examined in this study bubbles have become entrapped in the post-entrapment regime during the cavity collapse phase. These bubbles form via a slightly different mechanism than the bubbles in the primary bubble entrapment regime thus the bubble formation in the post-entrapment regime is labelled as secondary bubble entrapment after Liow (2001). All of the secondary bubbles observed from this study are plotted against impact Froude number in Figure 6.10.

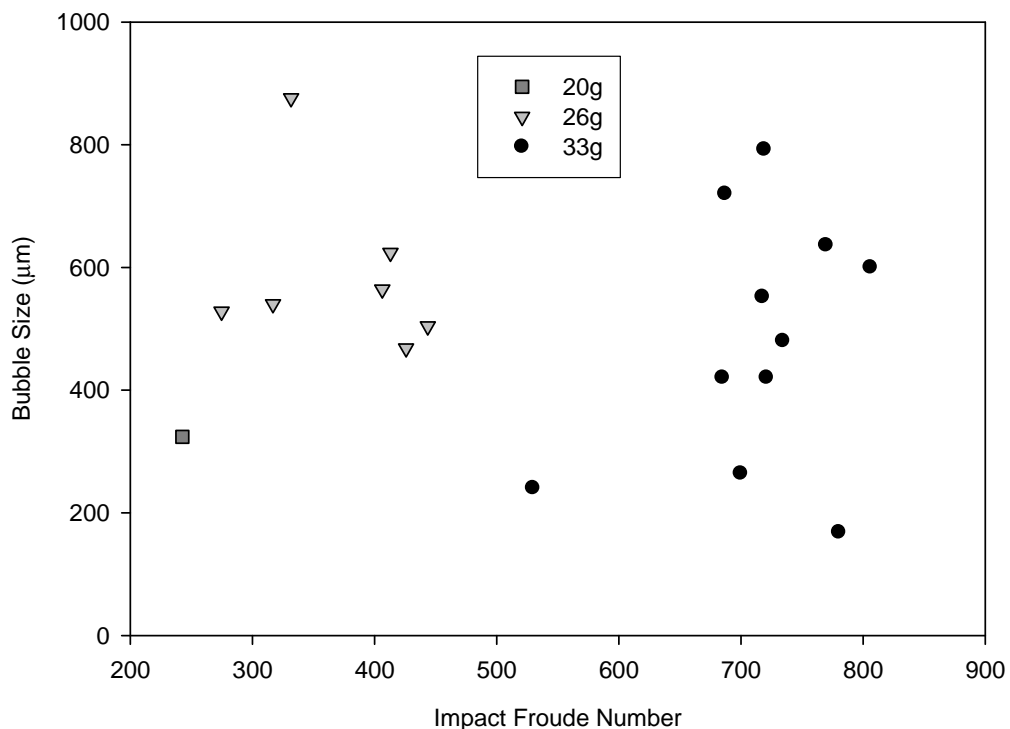


Figure 6.10 Secondary bubble size versus impact Froude number

From Figure 6.10 a highly variable secondary bubble size distribution can be seen. Not only does the bubble size vary markedly across the regime but also the Froude number separation between cases is also variable. Secondary bubble formation may or may not occur for impacts of exactly the same height. This somewhat random nature of the phenomena has led other researchers to call it irregular entrainment. An explanation on how these bubbles form and the reasons behind the stochastic formation behaviour needs to be addressed. To achieve this goal a series of images showing the final stages of secondary bubble formation are shown in Figure 6.11, Figure 6.12 and Figure 6.13.

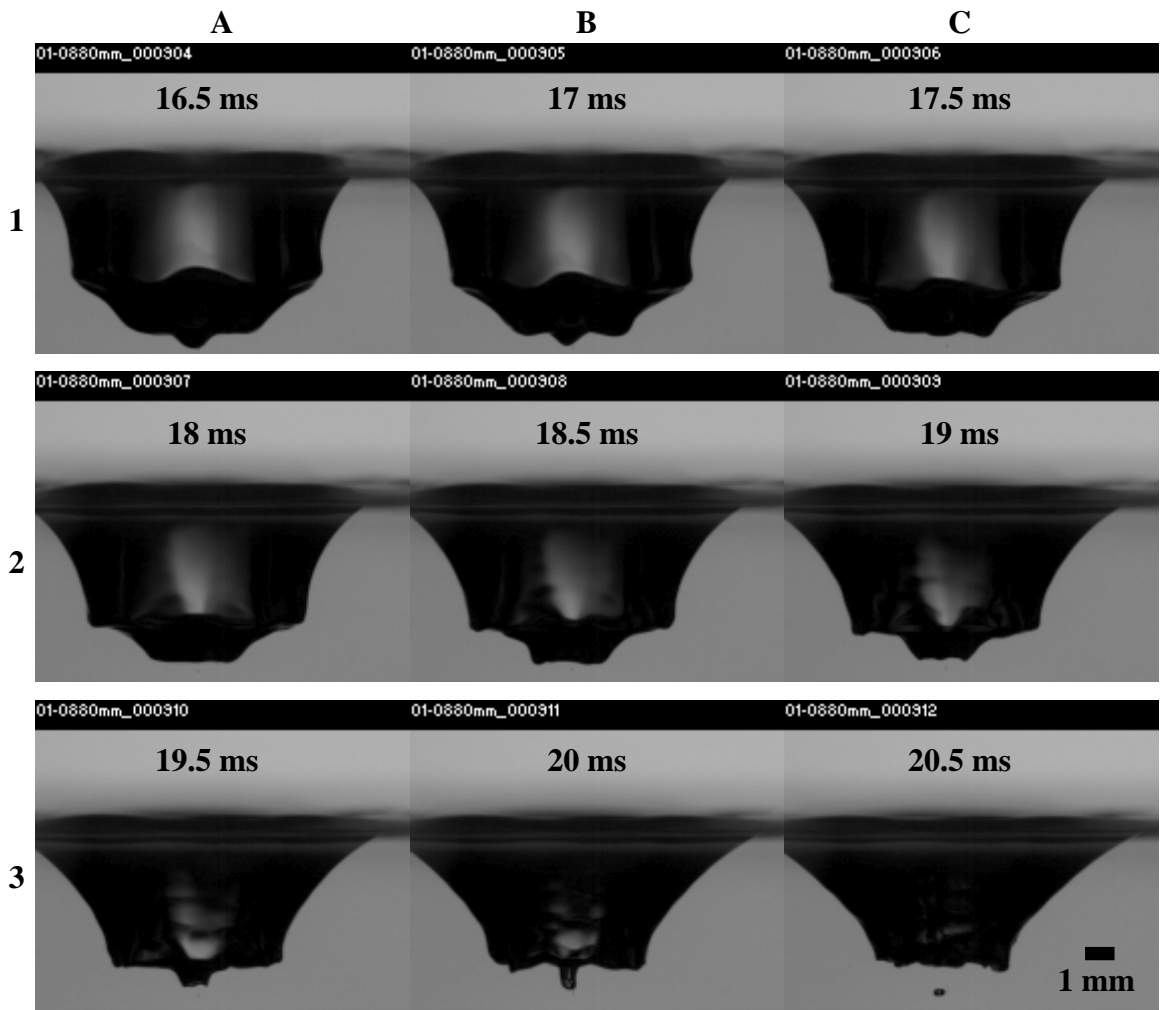


Figure 6.11 An example of secondary bubble entrapment in the post-entrainment regime ($Fr = 721$, $We = 410$, $Re = 7003$, $t_c = 0.54$) (2000 FPS)

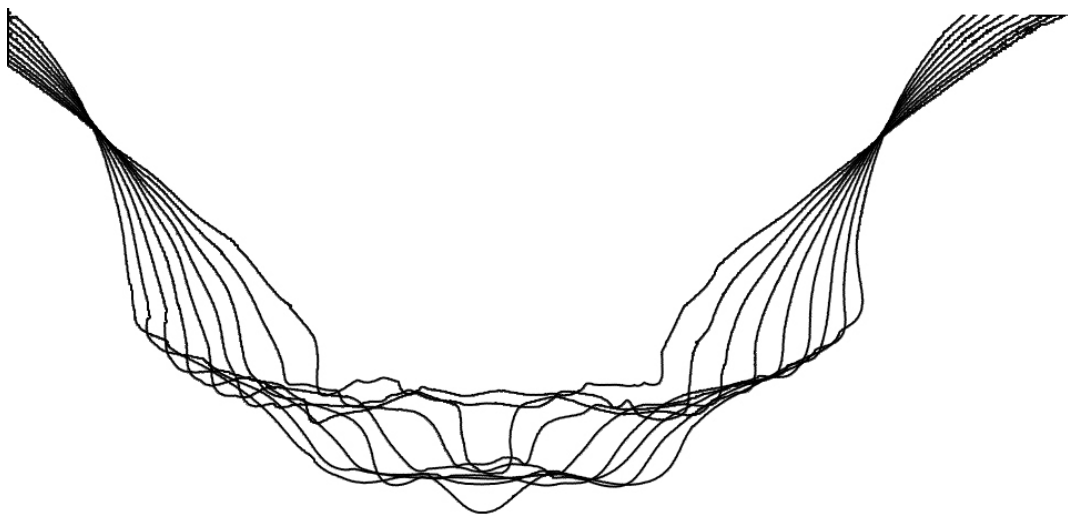


Figure 6.12 Cavity outlines from the image sequence shown above

Examining Figure 6.11 and Figure 6.12 shape of the cavity base is a complex shape. Initially in frame (A1-B1) the tip of the cavity base along the axis of symmetry has a protrusion. In frame C1 this protrusion retracts back into the cavity leaving what appears to be a flat base. The base of the cavity continues to come inward in the next four frames (A2-A3). Since there is little or no flow driving the cavity base upwards these distortions can be attributed to surface tension driven instabilities similar in nature to what was observed in section 6.4.2. Also during this time, capillary waves begin to appear on the cavity's surface. In frame, B3 the stem at the cavity becomes cylindrical before breaking up to leave a bubble entrapped (C3). It is clear that surface tension driven instabilities combined with the effects of complex 3D capillary waves converging at the base are forming a cylindrical stem. To gather more information on the bubble entrapment process a series of down cavity image sequences will be examined (Figure 6.13). Initially the tip of the cavity is pointing downwards. In frame B2 capillary instabilities acting on the cavity base act to turn the cavity base upward. The tip of the cavity reaches maximum amplitude in C2 before reducing in amplitude over frames A3-B3. As the cavity tip reduces in amplitude, the capillary waves converge at the base due to geometric focusing. In frame C3 the tip of the cavity is now directed downwards as the cavity begins to close. This enables a bubble to become entrapped (B4). Moments after the bubble has become entrapped an upward jet begins to form and the base of the cavity becomes dominated by a complex series of waves. In short, the process of secondary bubble entrapment can be described as a complex interaction of surface tension driven instabilities and capillary wave focusing. The critical element to ensure secondary bubble entrapment is that the tip of the cavity must be directed downwards as the capillary waves converge at the base. In all cases where the base of the cavity near the axis of symmetry was directed upward as the capillary waves converged at the base, no bubble was entrapped. Since the direction of the cavity tip is governed by an instability it is quite random as to which direction it will take, thus leading to the rather stochastic behaviour of the secondary bubble entrapment.

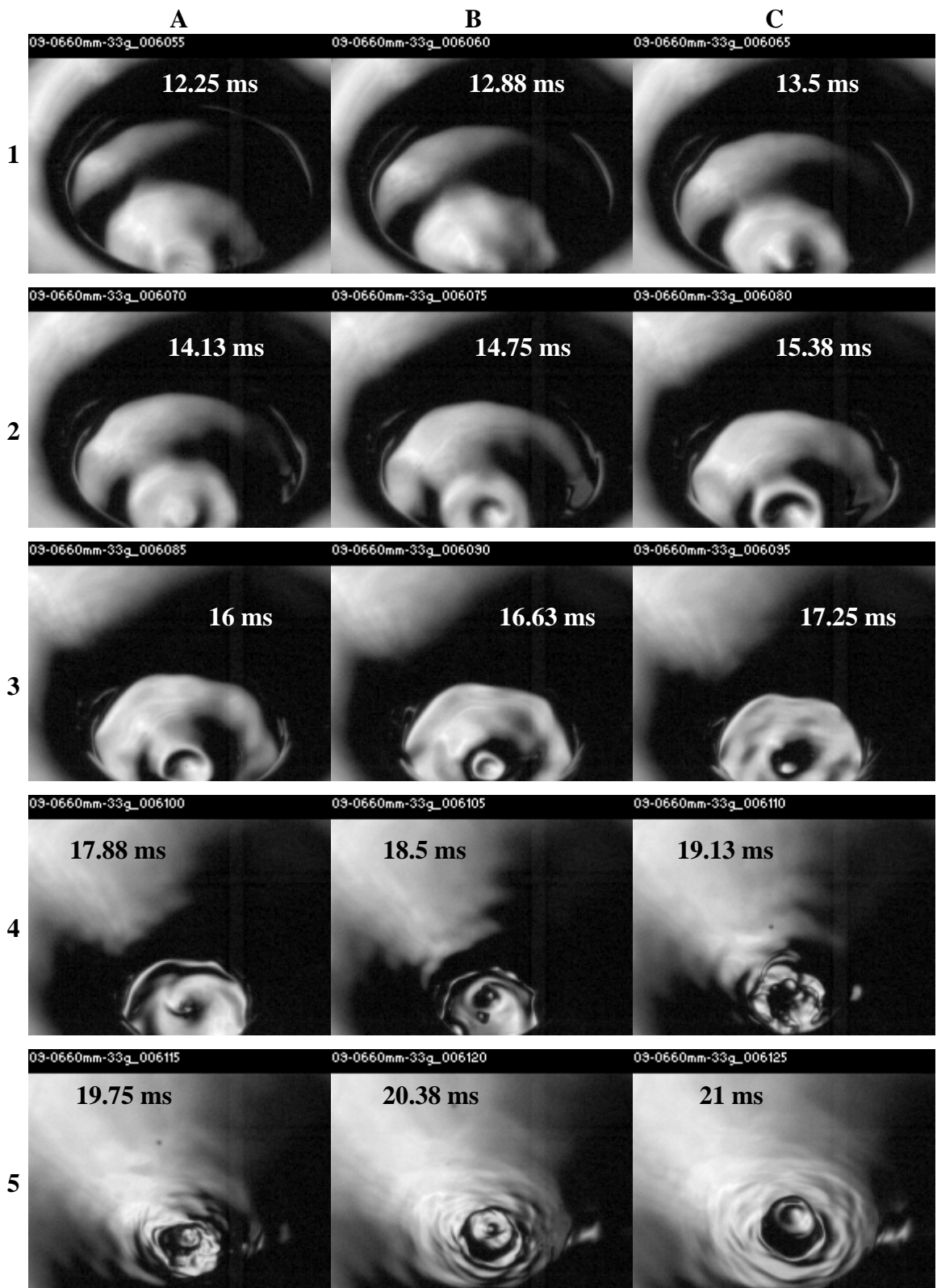


Figure 6.13 Down cavity image sequence for 33g-09-660mm (8000 FPS) showing capillary wave convergence (Estimated impact conditions $Fr = 560$, $We = 318$, $Re = 6169$, $t_c = 0.61$)

6.4 Microbubbles from thin film thinning

In Chapter 3 two different types of microbubble formation were shown to occur at low impact velocities and thus form the primary microbubble formation regime. Rupture that is due to a rapid expansion of the film and rupture due to the slow drainage of the film. In this section, the goal is to gain a deeper understanding of both these processes and attempt to estimate the volume of air that can be entrained by each mechanism.

6.4.1 Microbubbles from rapid film thinning (Mesler type)

To gain further insight into the break up of the air film the framing rate was increased in excess of 27 000 FPS so the actual moment of rupture could be captured. Figure 6.14 shows an image sequence of the air film break up. In Figure 6.14 the air lined cavity reaches a maximum depth in B1 before expanding out horizontally (C1-A3). The air film stretches and thins until it ruptures. The first sign of film rupture can be seen in B3 where the film on the far side of the cavity has begun to retract. The front side of the film begins to roll up in D3 leaving a trail of small bubbles between 12 and 60 μm in diameter. The final fragment of the air film forms a relatively large bubble 192 μm in diameter. The film itself retracts with a velocity of approximately 4 m/s.

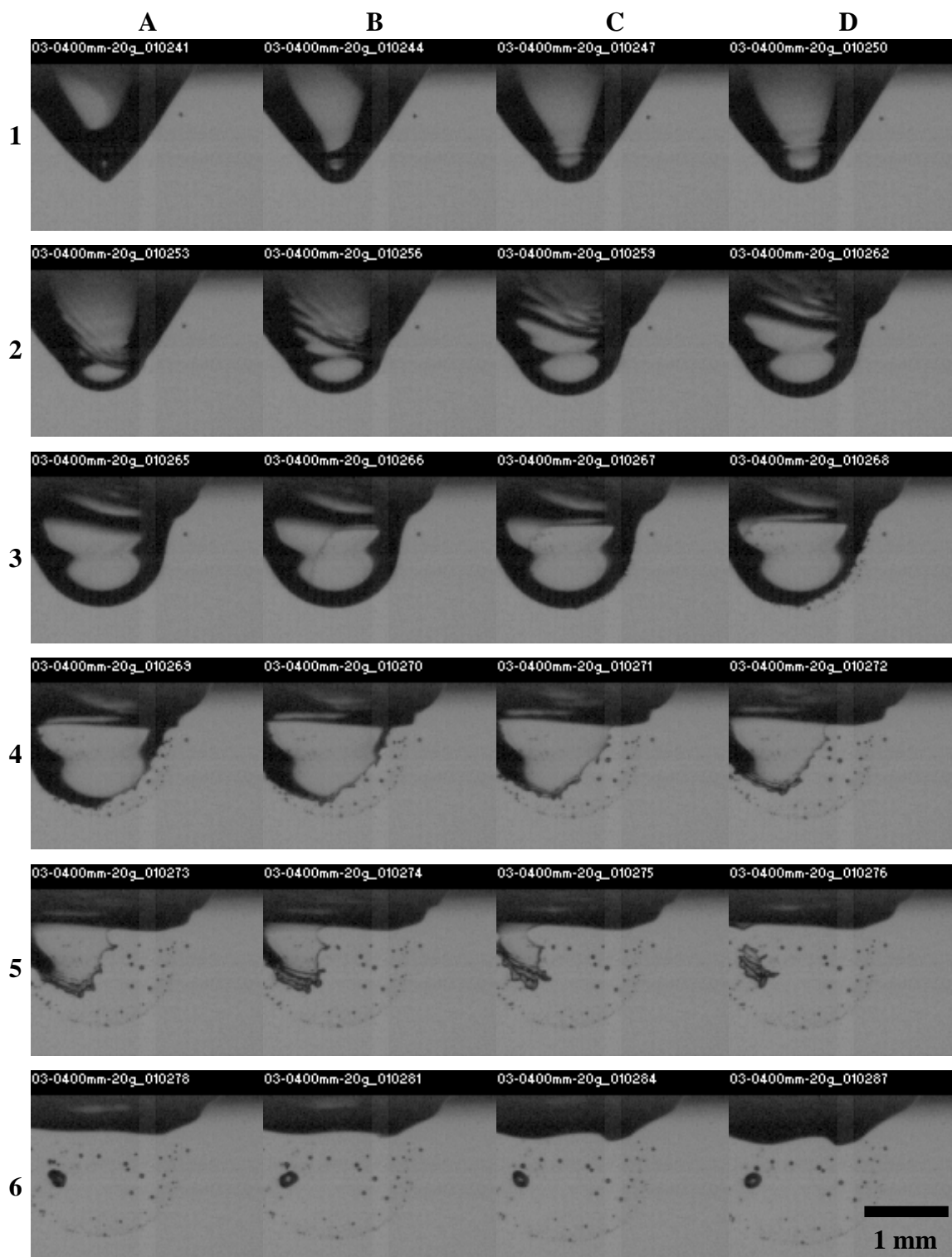


Figure 6.14 Air film rupture due to a rapid thinning of the film (Impact conditions of drop not captured) (27175 FPS)

When the film does not rupture during expansion the air lined cavity retracts and the impacting drop is thrown above the free surface before coming to rest (Figure 6.15). After the drop returns to the surface it floats for a period of time before coalescing. This leads to the coalescence cascade and a new type of bubble entrapment that will be described in 6.4.2. Thus, the critical factor in inducing Mesler type microbubble formation is that the drop must contain enough energy to expand the air film to an unstable thickness before the cavity has reached maximum depth.

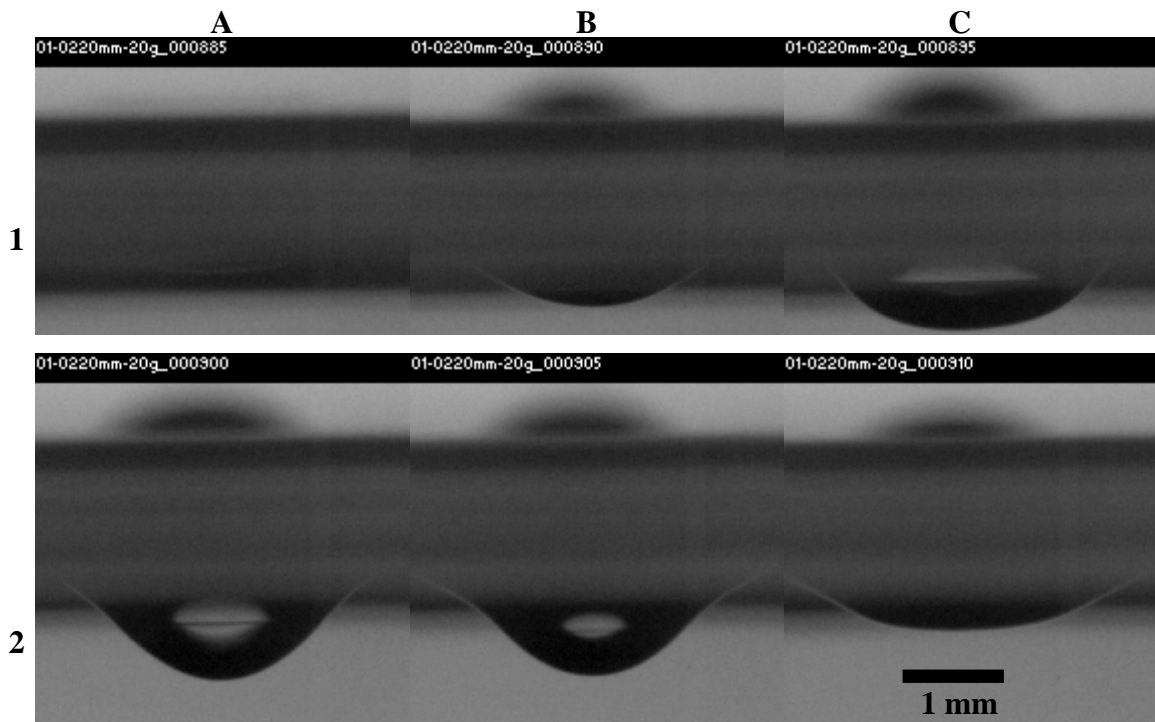


Figure 6.15 An example of the thin film not rupturing during initial impact ($Fr = 37$, $We = 18$) (3000 FPS)

The factors that contribute to the size and distribution of the microbubbles will now be examined. To aid the discussion here another two examples of thin film rupture are shown in Figure 6.16 and Figure 6.17. The first point to note from the image sequences shown in Figure 6.16 and Figure 6.17 is the difference in bubble size and bubble distribution. In Figure 6.16 most of the bubbles formed are at or below the resolution of the camera. This is the most common bubble size distribution seen in this regime. However, in Figure 6.17 the bubbles formed from the film rupture are similar in nature to the ones described in Figure 6.14. Examining the rupture velocity of the films, Figure

6.16 has a rupture velocity in the order of 9 m/s while Figure 6.17 has a velocity of 4.3 m/s indicating there is some correlation between rupture velocity and bubble size.

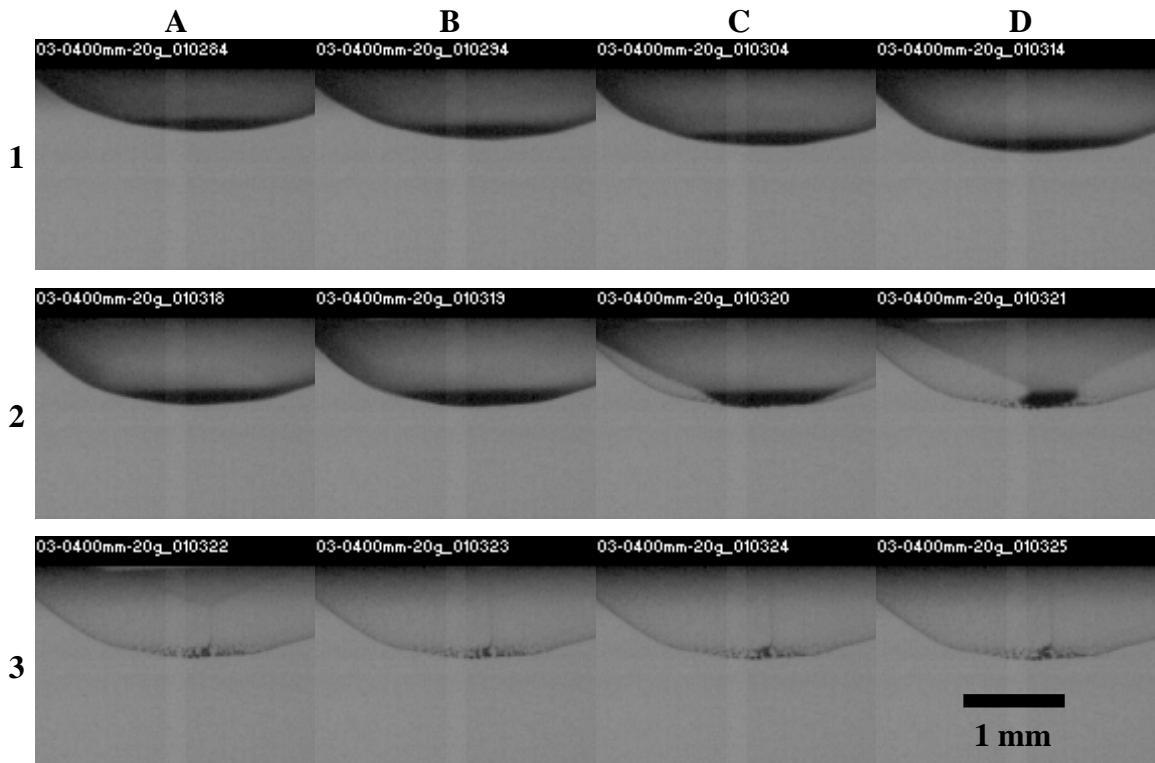


Figure 6.16 Air film rupture due to a rapid thinning of the film (Impact conditions of drop not captured) (27175 FPS)

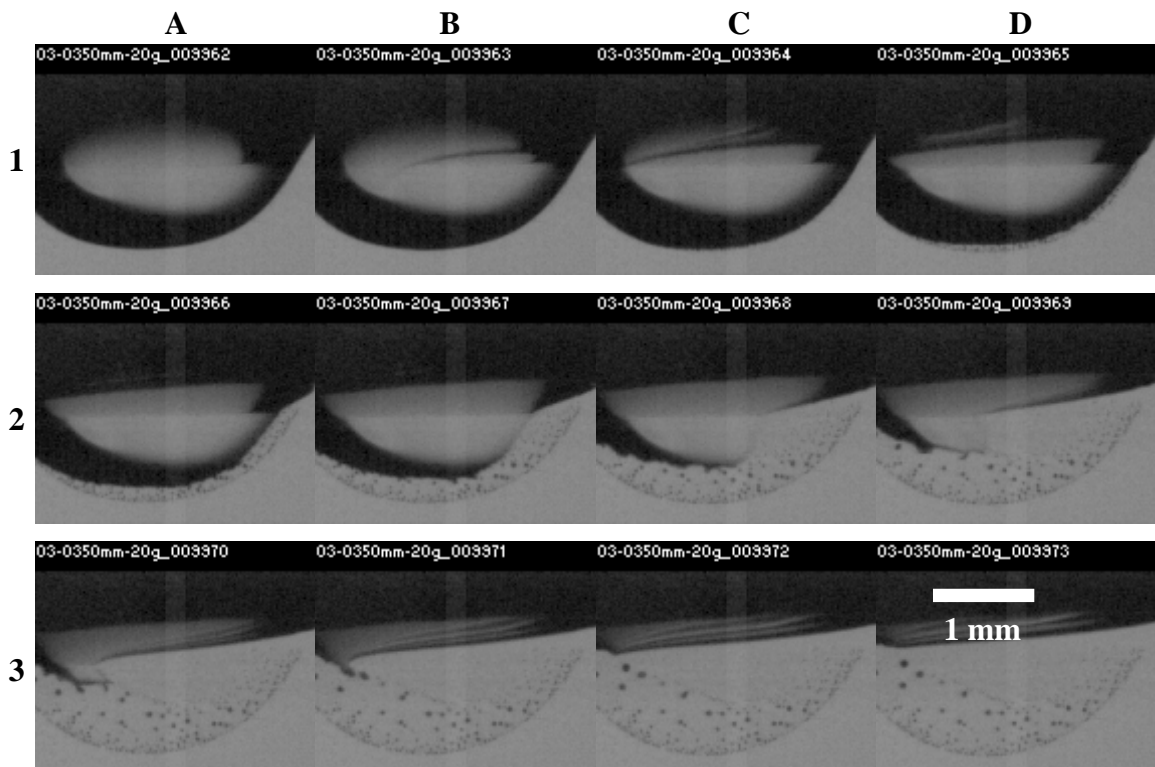


Figure 6.17 Air film rupture due to less rapid thinning of the film (Impact conditions of drop not captured) (27175 FPS)

The size and distribution of the bubbles formed by manually measuring and counting the bubbles from the captured images. The size and quantity of bubbles formed are recorded in Table 6.3. It should be noted that accurate measurement of large bubble swarms at the optical limit of the camera are exceedingly difficult. Therefore, counting the 12 μm bubbles are subject to large variations in the order 20-30% where thousands of them are formed.

Table 6.3 Microbubble size and quantity distribution for the 20g-03 data set

Height (mm)	192 (μm)	84 (μm)	72 (μm)	60 (μm)	48 (μm)	36 (μm)	24 (μm)	12 (μm)	Total Volume (mm^3)	Rupture Velocity (m/s)
275	-	-	-	5	-	-	-	4000	0.034	17.0
300	-	-	-	-	-	16	18	3000	0.030	9.1
325	-	-	-	-	18	8	18	3000	0.037	9.7
350	-	2	2	3	5	9	50	100	0.019	4.2
400	1	-	-	3	7	11	23	60	0.042	4.0

Examining Table 6.3 there clearly exists some relationship between rupture velocity and the size and distribution of bubbles formed. The reason for this behaviour is related back to the thickness of the film. Surface tension drives the retraction of the thin film and the magnitude of the force is dependant of curvature. In the case of thinner films the curvature is greater resulting in much more rapid retraction velocities. For the thicker films the curvature is less so the retraction velocity is less. Additionally thicker films will tend to produce larger bubbles while thinner films will produce smaller bubbles. The relationship between film thickness and rupture velocity will be used to determine the quantity of air entrapped more accurately in section 6.5.3.

6.4.2 Microbubbles from slow film drainage

In Chapter 3 an example of the microbubble formation from the rupture of the air sheet supporting a drop was shown. An enlarged image sequence of the film rupture is shown in Figure 6.18. The drop in this case is approximately 2 mm in diameter and rests on the surface for over 230 ms before partially coalescing. The actual moment of film rupture is not fully captured but occurs approximately between Figure 6.18 (B1) and Figure 6.18 (C1). The rupturing of the film allows the fluids to coalesce and this triggers a capillary wave which travels up the drop and can be seen in Figure 6.18 (B2).

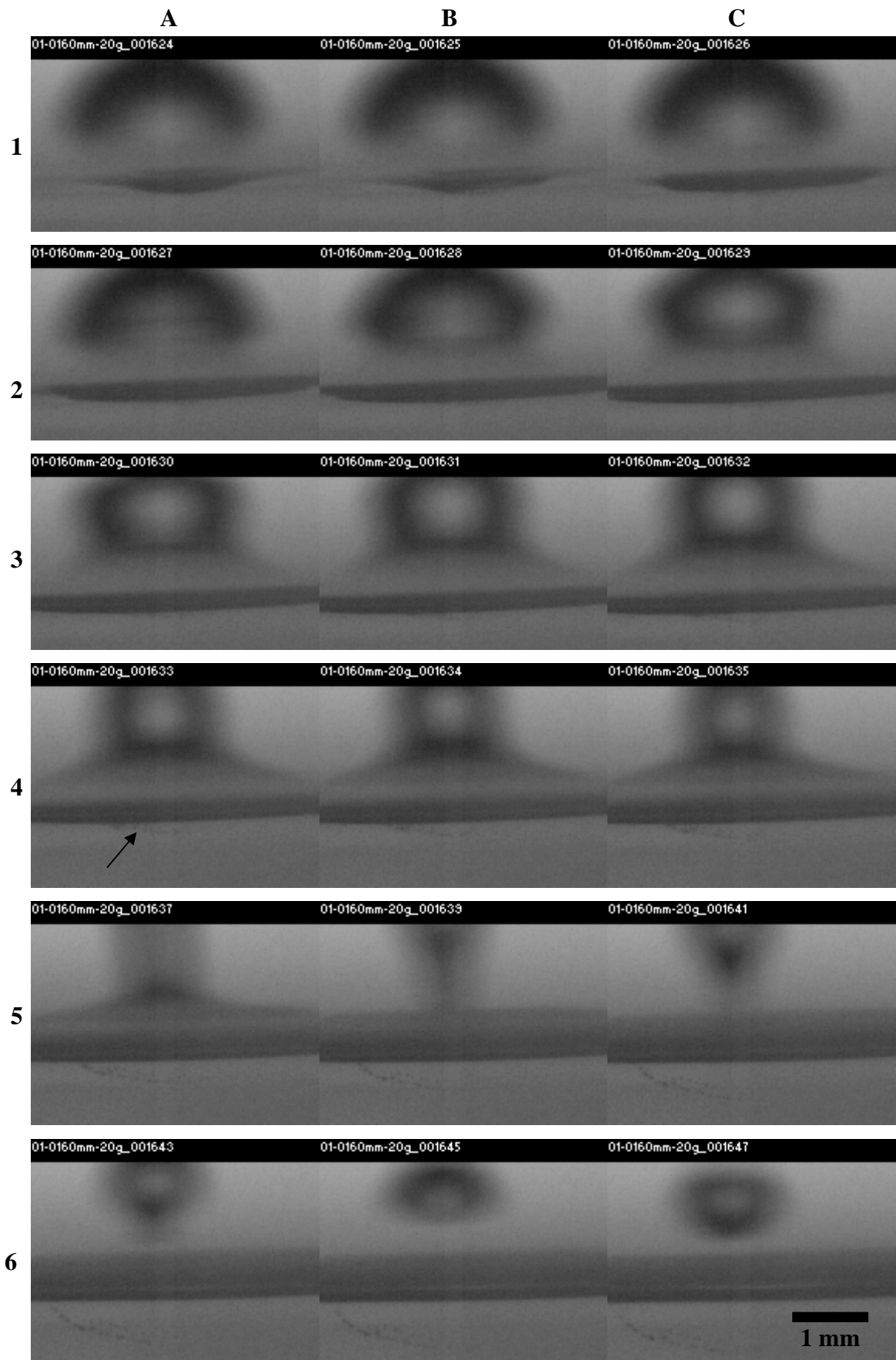


Figure 6.18 Rupture of the air film supporting a floating drop (3000 FPS)

The capillary wave distorts the drop into a cylindrical shape before pinching off a secondary drop. The bubbles resulting from the break up of the supporting film come into view in Figure 6.18 (A4). All of the bubbles formed in this example are below 24 μm in diameter. The break-up of the film supporting these drops has been observed down to drops of approximately 1 mm in diameter. Below this size range the film supporting the drop is extremely small and probably forms bubbles that are below the optical resolution used in this study. This is demonstrated in the next image sequence where the coalescence of secondary drop formed in Figure 6.18 occurs.

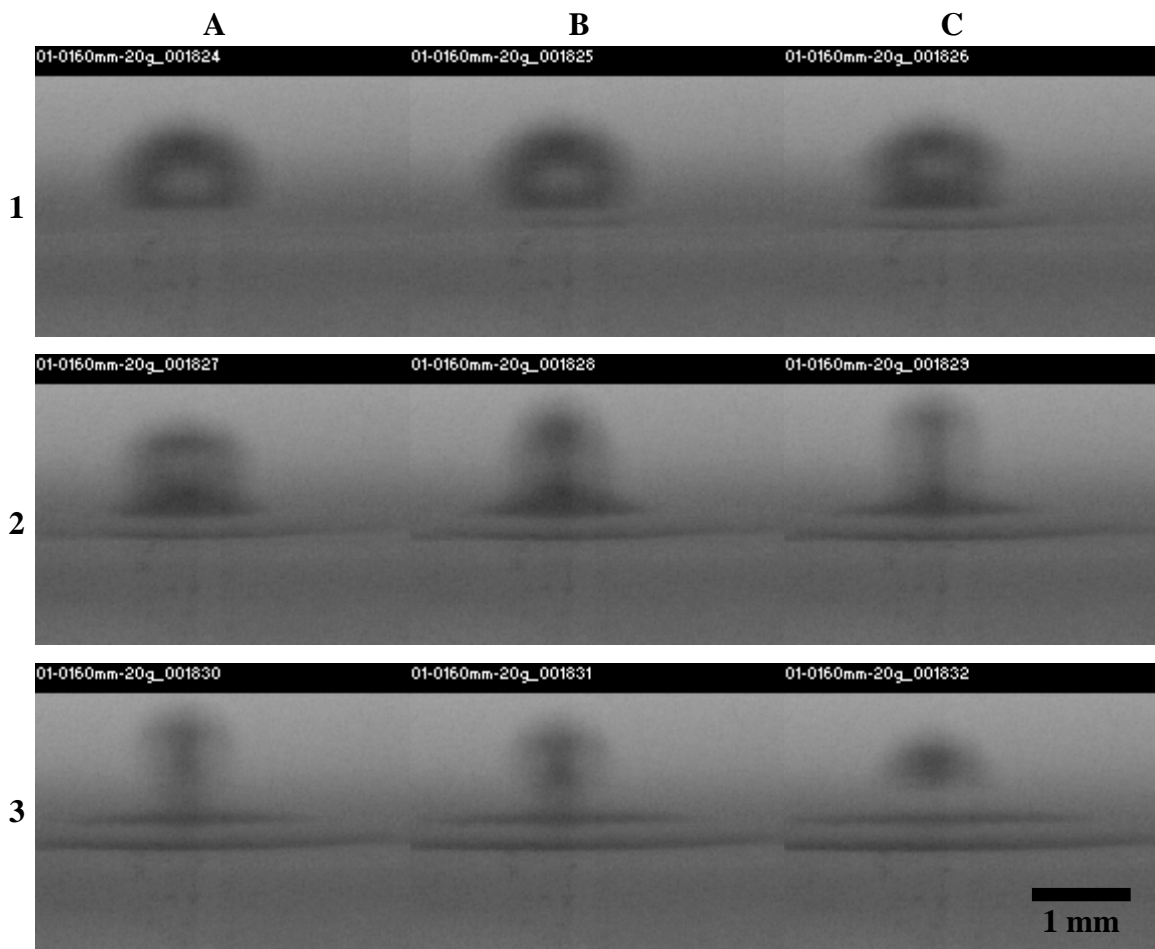


Figure 6.19 Second stage in coalescence cascade (3000 FPS)

In the image sequence shown in Figure 6.19 the film begins to rupture in frame B1. As the drop coalesces a capillary wave travelling up the drop forms another secondary drop. In now of these images the formation of microbubbles from the film rupture are not discernable. This is likely due to the film being so thin that the drops formed cannot be detected.

6.5 Air Film Formation and Rupture

6.5.1 Mechanism of formation

After extensively investigating the types of microbubble formation mechanisms it is clear they share many common features. In all cases, the rupturing of a thin gas film is the precursor to the creation of the microbubbles. The remaining question to be answered is what is origin of the thin gas films? The logical answer to this question would be the formation of an air cusp or sheet moments before impact. The actual formation of the air sheet is not actually captured in any images gathered from this series of experiments. However, the formation of the air sheets can be inferred from other observations. Numerical simulations by Mehdi-Nejad *et al.* (2003) have shown that a pressure field is propagated ahead of a liquid drop impacting on a liquid surface. If the pressure field is strong enough the liquid surface should become slightly deformed. This phenomenon has been observed when a large bubble rises up to the free surface. As a bubble approaches the surface, a pressure field is propagated ahead of the rising bubble due to the higher pressure contained within the bubble from surface tension. This in turn causes a deformation of the free surface. In the case of an impacting droplet on a liquid surface one would expect the pressure field propagating at the speed of sound ahead of the falling drop to behave in a similar way. This would induce a deformation of the free surface allowing a portion of air to become entrapped between the two surfaces.

The question now becomes how is the air constrained between the two surfaces over an extended period of time so that the air film stays entrapped during cavity expansion and while the drop floats? From this study it is not entirely clear what forces are keeping the air between the two liquid surfaces during the dynamic impact. Thoroddsen *et al.* (2003) and Pikhitsa and Tsargorodskaya (2000) suggest that viscous forces are responsible constraining the air between the two liquid layers. Looking at the Reynolds number for the flow of the air contained in the film can give some insight into the forces dominating the process. If the characteristic length scale is the thickness of the film ($\approx 1 \mu\text{m}$), the velocity scale is the impact velocity of drops in this region ($\approx 0.6 \text{ m/s}$) and using standard properties for the viscosity and density of air, the Reynolds number is 0.033. This indicates viscous forces will dominate during the initial formation of the

film. However, more work needs to be conducted in this area to support these arguments.

6.5.2 Limits on microbubble formation

In this section, data on the impact conditions required to form microbubbles from both the rupture of the thin film during expansion and floating drops is presented. The impact conditions for the secondary drops formed in this study are shown in Figure 6.20. Drops falling in the primary vortex ring regime are shown for reference.

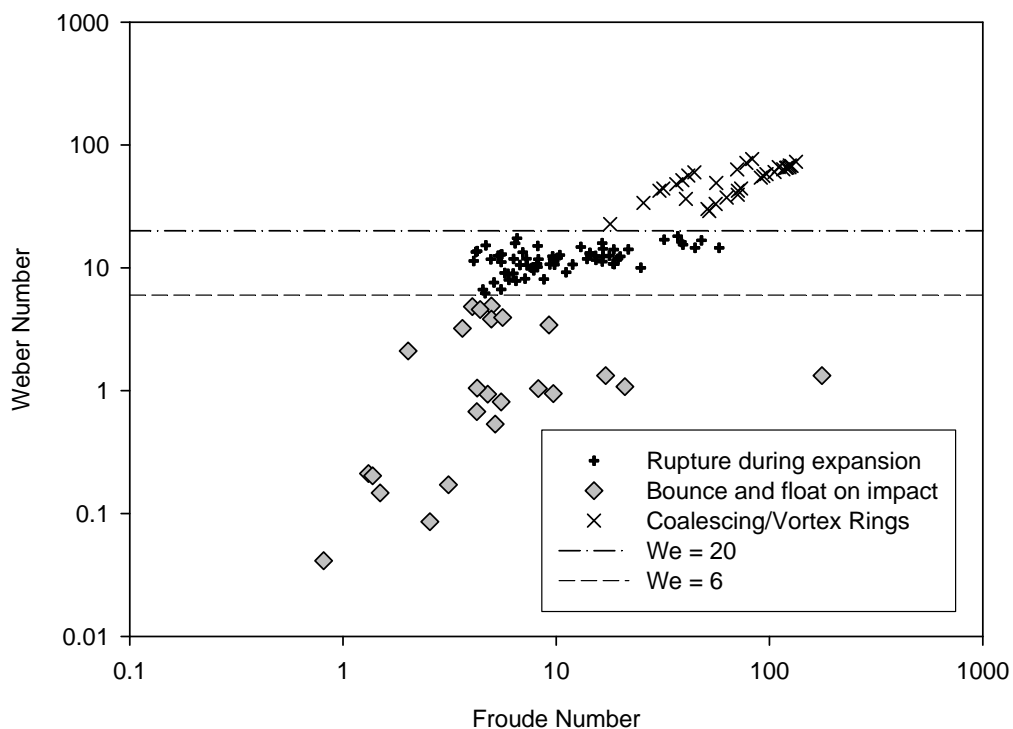


Figure 6.20 Dimensionless parameters of secondary drops as they impact the liquid surface

Examining Figure 6.20 it can be seen that the microbubble entrapment regimes have a very strong Weber number dependence on when they will form. The transition between the rupture of the thin film during expansion and not rupturing during expansion is governed by a $We = 6$. The upper limit on the mass formation of microbubbles is given by a $We = 20$. It appears that the criteria for film breakup is a balance between inertial and surface tension forces. If the inertial force associated with the impact can overcome the surface tension forces holding the film together, the film will break up.

6.5.3 Estimating quantity of air entrapped

The easiest method to estimate the quantity of air entrapped is to simply measure the diameter of all the bubbles formed. While this is sufficient for bubbles $> 30 \mu\text{m}$, the smaller bubbles that are near and below the minimum optical resolution become impossible to measure. In fact, the only reason most of the microbubbles becomes visible is by the virtue there being thousands of them that form microbubble clouds. Therefore, a more accurate method of determining the quantity of air entrapped is required. Understanding the shape and therefore volume of the thin film is the first step required. It has already been shown how the air film layer must extend to all points between the two liquid surfaces to prevent coalescence. Thus, the air film can be assumed to take the shape of a thin walled hemi-spheroid. The total volume of air entrapped can now be estimated by the following equation,

$$V = \frac{2}{3}\pi[a^2b - (a-h)^2(b-h)] \quad (6.1)$$

Where a is the major radius (cavity half width), and b the minor radius (cavity depth) and h the thickness of the film. The major radius and minor radius can be easily measured from the images. However, experimentally estimating the film thickness is almost impossible. An estimate of the film thickness based on rupture velocity can be obtained. Previous theoretical work on the rupture of thin films by Pandit and Davidson (1990) have shown that rupture velocity of a thin liquid film can be predicted by

$$v = \sqrt{2\sigma / \rho h} \quad (6.2)$$

Thoroddsen *et al.* (2003) used a similar equation to verify that these relationships held for thin gas films in water. Therefore, a theoretical thickness of the film can be calculated based on the velocity extracted from the images. Using equations 6.1 and 6.2 total volume of air entrapped by the rupture of thin films can be estimated.

Table 6.4 Estimated and measured values of air volume entrapment due to thin film rupture during expansion

Height (mm)	Rupture Velocity (m/s)	Estimated Film Thickness (μm)	Expected volume entrapped (mm^3)	Measured volume entrapped (mm^3)	% Difference
275	17.0	0.50	0.006	0.034	460%
300	9.1	1.75	0.022	0.030	40%
325	9.7	1.56	0.035	0.037	6%
350	4.2	8.14	0.071	0.019	74%
400	4.0	9.23	0.037	0.042	15%

Using the above procedure, the quantity of air entrapped from the break up of the film supporting floating drops can be estimated. However, in all of the examples captured in this study it was not possible to directly measure the rupture velocity. Only a rough estimate for the film thickness based on the size of the bubbles produced can be made. For film break-ups that left behind bubbles with sizes in the range of 24 μm the film thickness is assumed to be approximately 1 μm . This estimation is consistent with calculated values of the film thickness from Table 6.4 where similar bubble size distributions were observed. Estimating the entrapped volume by direction measurement was also extremely difficult and could only be partially achieved in two cases. Thus, one would expect significant errors in the calculated values shown in Table 6.5.

Table 6.5 Estimated entrapped air volumes for floating drops

Study Item	Height (mm)	Estimated Film Thickness (μm)	Estimated volume entrapped (mm^3)	% of original drop volume
20g-01	200	1	0.00105	0.010
20g-01	220	3	0.12617	0.125
20g-01	160	1	0.00092	0.009
26g-01	420	1	0.00018	0.003
26g-04	300	1	0.00088	0.012

6.6 Summary

This chapter has attempted to identify the different modes of bubble entrapment during liquid-liquid impacts. Some of the physical forces that affect the formation of the bubbles have been explained. For practical purposes the quantity of air each mode of bubble entrapment can entrain has been described. This is summarised in Table 6.6 where the quantity of air entrapped is described as a percentage of the original drop volume.

Table 6.6 Entrapped air volume as a percentage of original drop volume for all bubble entrapment mechanisms

Bubble formation mode	Regimes	Upper Limit Lower Limit	% Min-Max	% Average
Thoroddsen Bubbles	Primary vortex ring, Pre-entrapment jetting, Primary bubble entrapment, Post-entrapment	Highest Impact* We > 20	0.0018- 0.0063	0.0029
Primary Bubble Entrapment	Primary bubble entrapment	We < 41.5Fr ^{0.253} We > 36.2Fr ^{0.186}	0.16-6.45	3.68
Secondary Bubble Entrapment	Post-entrapment jetting regime	Highest Impact* We > 97.2Fr ^{0.183}	0.057-6.03	1.62
Film Thinning (rapid expansion)	Primary microbubble formation regime	We < 20 We > 6	0.1-0.7	0.3
Film Thinning (slow drainage)	Primary microbubble formation regime	We < 6 Oh > 1	0.003-0.125	0.03

* indicates that the phenomena was observed in the highest velocity impacts in this study. Thus no firm upper limit can be placed on the phenomena for the results of this study

Briefly examining Table 6.6 it can be seen that primary and secondary bubble entrapment can entrap the largest quantity of air. However, the bubbles formed from these modes of entrapment are quite large and thus have strong buoyancy forces that drive them toward the free surface. At the free surface these bubbles burst, thus making them undesirable for oxygen exchange within the bulk fluid. The next highest mode of bubble entrapment comes in the form of the rupture of thin films due to rapid expansion. The bubbles formed in this regime are extremely small and have been shown to be driven deep into the bulk fluid enabling them to completely diffuse. The other

three modes of bubble entrapment Thoroddsen and floating drop rupture only entrap minor amounts of air compared to the film rupture due to rapid expansion. Methods on how to accurately estimate the volume of air that can become entrapped from this bubble entrapment mechanism has been presented.

In terms of physics driving the formation of bubbles during cavity collapse it has been postulated that for the primary bubble entrapment regime, the flow around the base of the cavity at the time bubble pinch off is vital in determining what size and shape bubbles are formed. Towards the upper end of the primary bubble entrapment region a distinct area double bubble entrapment was observed and detailed. Here surface tension instabilities interact with the inertia of the surrounding flow to break the cavity stem into multiple bubbles. The somewhat stochastic behaviour of the instability leads to a certain element of randomness in how and if multiple bubbles become entrapped in this region. Finally, secondary bubble entrapment were examined. This phenomenon was postulated to occur due to a combination of surface tension driven instabilities interacting with capillary driven waves converging at the base of the cavity. The effects of both the capillary waves and capillary instabilities make the phenomena rather random in when it will occur and is reflected in experimental results.

CHAPTER 7 - SUMMARY AND CONCLUSION

7.1 Splashing Morphology

In this thesis, a coherent picture of the splashing behaviour that can result from liquid-liquid impacts has been presented. Chapter 3 sought to unify all current knowledge in this field into a series of diagrams for easy practical use. Figure 3.2 allows the reader to identify any phenomena of interest for a given application. While Figure 3.49 and Figure 6.20 can be used to identify the impact conditions at which each phenomena occurs so that it can be avoided or promoted depending on the application.

In terms of flow regimes it was discovered that the description of the flow in terms of bouncing, floating and coalescing drops is an overly simplistic view. Many flow phenomena are interrelated and phenomena like vortex rings, jetting and bubble entrapment can occur across the entire spectrum at different points. Thus the flow regimes were classified into six distinct regions based on the flow behaviour that was most prominent in that region. These flow regimes were labelled the

- Total coalescence regime
- Primary microbubble formation regime
- Primary vortex ring regime
- Pre-entrapment jetting regime
- Primary bubble entrapment regime
- Post-entrapment jetting regime

In the total coalescence regime, the drop coalesces without any significant cavity formation, jetting, bubble entrapment or vortex ring formation. Drops that fall into the primary microbubble formation regime coalesce because of the supporting air film rupturing and forming tens or thousands of small microbubbles that permeate into the bulk fluid. This regime is useful to promote oxygen exchange in the bulk fluid. In the primary vortex ring regime, no significant jetting or bubble entrapment occurs but large coherent vortex rings can be formed which penetrate deep into the bulk of the fluid. The pre-entrapment jetting regime can form high velocity jets without any bubble entrapment. This regime may be desirable for applications where high velocity drops

are required without having any audible noise or bubble entrapment. The large bubbles formed during primary bubble entrapment tend to burst at the free surface which produced jets with small high velocity drops. These small drops may cause hazardous mist formation in some industrial applications and should be avoided. The final regime documented in this thesis is the post-entrapment jetting regime. Here the thick jets produce large slow moving secondary drops that can fall into the primary microbubble entrapment regime.

7.2 Cavity Behaviour

High speed PIV has been used to image the flow field around the expanding and collapsing cavity. Based on this data, a six stage flow model was proposed.

- Stage 1: Expansion and wave swell growth
- Stage 2: Peak wave swell height
- Stage 3: Wave swell drainage
- Stage 4: Cavity base stagnation
- Stage 5: Vortex formation
- Stage 6: Flow convergence along centreline

The critical elements in this flow model depend on the behaviour and development of the wave swell and the vortex that forms mid way down the cavity and acts to collapse the cavity. The draining of the wave swell was shown to provide the fluid that acts to collapse the cavity. Using 2D cavity outlines the centre of the vortex was shown to remain stationary during collapse forming a stationary line about which the entire cavity rotates about. The variation of the stationary line in both the horizontal and vertical directions was also described. For impacts of the same drop size the depth of the stationary line below the free surface was essentially constant. While the variation of the width was shown to scale with the Froude number of the impact. However, no theoretical explanation could be given for this scaling. Finally, three flow convergence conditions were put forward to explain the different jetting modes.

7.3 Jetting

In the study of the jetting behaviour in liquid-liquid was described in detail. A distinct regime of pre-entrapment jetting was observed along with the first direct experimental evidence of downward jets associated with bubble entrapment has been presented. More extraordinarily the downward jets were found to break up and form drops inside the large entrapped bubbles. These drops then coalesce with the bulk fluid and in certain cases form a second entrapped drop. The physics that dictate jetting behaviour of the jets was also explored. This was done by examining how the flow converges at the base and by measuring the retraction velocity and acceleration of the cavity base. In some cases the acceleration of the cavity was measured to be as high as 90 000 g while peak drop exit velocities were measured as high as 30 m/s. The reason for all high speed jetting can be attributed to a stagnation point that form at the base of the cavity. This was found to be due to the way the fluid converges at the base during cavity collapse. It was also shown that there is a direction correlation between the retraction velocity of the cavity and drop exit velocity.

7.4 Bubble Entrapment

In this study the most comprehensive study of the bubble entrapment modes and the quantity of air they entrap has been described. The most practical spin off from this work involves its immediate application in water aeration. In chapter 6 the production of microbubbles from secondary drops that pinch off thick jets has been identified as the best source of bubbles that can diffuse into the bulk fluid. Therefore, if one wanted to maximise oxygen exchange with the bulk fluid it would be most efficient to form thick jets which in turn form drops with Weber numbers between 6 and 20. Operating in this range it would be expected that the secondary drops falling within this region would entrap 0.3% of the original drop volume on average.

7.5 Conclusion

In closing the purpose of this thesis was to broadly canvas the splashing morphology of liquid-liquid impacts along with understanding the physics that drive specific phenomena including cavity formation and collapse, jetting and bubble formation. These objectives have been largely achieved in this study and answers to some of the

100 year old questions first posed by the pioneers in this area have been addressed. However, as many questions were answered in this study, many more questions have arisen from this work. These topics form the basis for future work that needs to be conducted in this area.

7.6 Future Work

Splashing Morphology

- Explore flow regimes at higher impact velocities greater than 4 m/s up to the terminal velocity of approximately 8 m/s
- Conduct studies with different fluid properties to investigate the influence of surface tension and viscosity to see how the limits on the splashing regimes change

Cavity Formation

- Carry out a deeper study into the behaviour of the stationary line flow physics that allow it to form
- Use higher resolution and higher framing rate PIV to detect the initial stages of vortex ring formation
- Examine the influence of the downward flow convergence on the development of strong coherent vortex rings

Jetting

- Understand why there is a limit on the drop velocity/size ratio
- Use higher optical resolutions to see if smaller drops $< 12 \mu\text{m}$ in diameter are formed by the high-speed jets
- Need to investigate downward jets more thoroughly to understand why the drop-in-bubble coalesces

Bubble formation

- Explore the acoustics of the drop in bubble coalescing
- Explore the acoustics of large multiple bubble formation in the upper region of the primary bubble entrapment regime

- Understand the physics of how the air sheet forms in microbubble formation regime
- Investigate the Oguz bubble ring formation to see if it does indeed occur
- Need more detailed studies of the mechanism that allows drops to float for prolonged periods